Reliability of using ASTER data in lithologic mapping and alteration mineral detection of the basement complex of West Berenice, Southeastern Desert, Egypt

Hatem Aboelkhair[1] · Ahmed Abdelhalim[2] · Zakaria Hamimi[3] · Majid Al-Gabali[4]

Abstract

The Neoproterozoic basement complex of Egypt outcrops in the Eastern Desert (ED) and southern Sinai, and is regarded to represent the northwestern continuation of the Arabian–Nubian Shield (ANS). The area west of Berenice has been given little attention, although it represents the key to understanding the geologic history of the South Eastern Desert and the entire ED. The present work is an integrated study using remote sensing (Advanced Spaceborne Thermal Emission and Reflection Radiometer (ASTER) data imagery) and field-structural data to assess their utility in lithologic mapping and in detecting alteration mineral zones with considerable accuracy. A false-color-composite image, color-ratio composite image, decorrelation stretch, mafic index (MI), and quartz index (QI) were used to discriminate and map the various rock units. Correlation of False-color images of the ASTER band combination (7, 3, 1) with previous lithological mapping studies of the study area allow preliminary discrimination of different lithologies and drawing a base map. Subsequently, ASTER band ratios tested (4/1, 3/1, 12/14) and (4/7, 4/6, 4/10) with the ground truth data were used to refine the base map and construct the digital detailed geologic map. Petrographically, the investigated rock samples show kaolinite, chlorite, and epidote in alteration zones. The spectral angle mapper (SAM)-supervised classification using reference spectra of the USGS spectral library was used for detecting alteration zones. For verification, total accuracy assessment was carried out to evaluate the band combination and band ratios used in the lithologic mapping. That reached to 85.01% for band ratio 4/1, 3/1, 12/14 in RGB.

Keywords Arabian–Nubian Shield · Basement complex · Berenice · ASTER · Remote sensing

Introduction

There is general agreement that the Arabian–Nubian Shield (ANS) represents the northern continuation of the East

✉ Hatem Aboelkhair
haboelkhair@du.edu.eg

1 Center of Space Research and Applications (CSRA), Damietta University, New Damietta, Egypt

2 Department of Geology, Faculty of Science, Cairo University, Giza, Egypt

3 Department of Geology, Faculty of Science, Benha University, Benha 13518, Egypt

4 Department of Geology and Environment, Thamar University, Dhamar, Yemen

African Orogen (EAO). The EAO is considered by many workers to represent a megasuture zone separating East and West Gondwana, formed due to the closure of a Pacific-sized Mozambique Ocean at about 550 Ma (Johnson et al. 2011). The ANS comprises Neoproterozoic basement lithologies outcropping in Western Arabia (Arabian Shield) and Northeast Africa (Nubian Shield). These lithologies uplifted since the Oligocene and younger times because of the Red Sea rifting (Stern 1994, 2002). The ANS is subdivided into tectonic terranes, separated along suture zones and megashears (high-strain zones). The Eastern Desert of Egypt (ED) occupies the northwestern sector of the ANS and is considered to represent a tectonic terrane, namely ED terrane (in some literatures, it is called Aswan terrane or Geref terrane). Several attempts have been made to map and classify the Neoproterozoic rocks outcropping in the ED (e.g., Hume 1934; Schurmann 1957; Akaad and El Ramly 1960; El Ramly 1972; Akaad and Noweir 1969, 1980; El Gaby 1988; El Gaby et al. 1990; Abdel-Khalek et al. 1992). When these

classifications were scanned, it was found that the exposed lithologies in the ED could be classified into four major rock groups: (1) gneisses, migmatites, and remobilized equivalents; (2) ophiolites and island arc assemblages; (3) Dokhan volcanics and Hammamat sediments; and (4) intrusives (granitoids and gabbro–diorite complexes).

The Advanced Spaceborne Thermal Emission and Reflection Radiometer (ASTER) sensor is an imaging instrument that was launched in December 1999 and provides medium spectral resolution data that enables geologic mapping and mineral exploration, particularly for areas with poor ground-based information (Di Tommaso and Rubinstein 2007). ASTER was launched by NASA and Japan's Ministry of Economy. The satellite was designed to obtain medium-resolution global, regional, and local images of Earth (Abrams et al. 2002). ASTER data consists of 15 bands which include a band from a second onboard sensor which points backward to create parallax (band 3B). Parallax is very useful for topographic mapping and creation of digital elevation models (DEM).

One of the main goals of geological remote sensing research especially in arid and semi-arid regions is the development of methods for mapping rock types and hydrothermally altered zones (e.g., Askari et al. 2018; Bedini 2019; Ninomiya and Fu 2018; Noori et al. 2019; Pour et al. 2019a, b, c; Pour et al. 2018a, b; Sheikhrahimi et al. 2019).

In ED of Egypt, many authors used the satellite images of the ASTER sensor for lithologic identification and geological mapping of basement complex (e.g., Asran et al. 2017; Hassan et al. 2017; Jakob et al. 2015; Amer et al. 2010; Gad and Kusky 2007), while other authors used ASTER images for exploration of gold occurrences (e.g., Ibrahim et al. 2016; Salem et al. 2016; Gabr et al. 2010, 2015; Amer et al. 2012; Zoheir and Emam 2012; Zoheir et al. 2019). Also, ASTER TIR data were used for exploring and mapping uranium and rare-metal-enriched albite granite (e.g., Aboelkhair et al. 2010; Elsaid et al. 2014).

The West Berenice area lies in the extreme South Eastern Desert (SED) of Egypt. This area has not been studied in detail before. It is included in the regional geologic map (scale 1:250.000) covering the Berenice topographic sheet. It is regionally mapped also by (Conoco 1987) (scale 500.000). This area shows most of the essential features of the SED, in terms of lithology and structural features. The aims of the present study are to use ASTER data imagery, along with ground truth, for accurate lithologic mapping in the study area and to locate alteration mineral zones as pathfinders for mineral exploration in the area of interest.

Study area

The study area is located in the SED, about 12 km to the west of the Ras Banas and Berenice port on the Red Sea Coast (Fig. 1). It lies in the arid to semi-arid regions of the SED and is characterized by a good exposure. As a result, the area is suitable for remote sensing-based investigation. It covers about 1213 km^2 collection of structurally and metamorphically complex rocks and bounded by the following coordinates: longitudes 35° 02′ 24.00″ to 35° 23′ 56.40″ E and latitudes 23° 48′ 36.00″ to 24° 6′ 0. 00″ N.

The study area is characterized by high to low relief topography, with elevations ranging between 9 and 1540 m above mean sea level. The topographic color-shaded map that resulted from the SRTM Worldwide Elevation Data (1 arc-second resolution) is shown in Fig. 2. It can be classified physiographically into three main terranes: Al-Hefery-Jabal Um Dalaq terrane, Jabal Um Junud-Jabal Kalalat terrane, and Jabal Abu Jurdi-Nasb Eiqat-Jabal Lahmi terrane. The Al-Hefery-Jabal Um Dalaq terrane occupies the eastern side of the study area. It has a low topographic relief where elevations are not exceeding 440 m. The Jabal Um Junud-Jabal Kalalat terrane extends from Jabal Um Junud in the central area to the southern area. The elevations in this terrane range between 440 and 880 m. The Jabal Abu Jurdi-Nasb Eiqat-Jabal Lahmi terrane occupies the NW of the study area. It has the highest elevation in the study area, reaching up to 1500 m.

Materials and methods

ASTER data

The ASTER image of the study area is Level-1B obtained from the Earth and Remote Sensing Data Analysis Centre (ERSDAC). The data were already radiometrically calibrated, geometrically corrected and scaled radiance at the sensor. A subset of the whole scene covering only the study area was extracted. The ASTER data were also projected to the UTM projection (WGS84 datum, zone 36N). Table 1 shows the characteristics of the selected ASTER scene.

Field data

More than 70 rock samples were collected using handheld GPS representing various lithologic units at several stations, and GPS waypoints for all sample locations were recorded (Fig. 3). The points of the collected site locations were converted into a GIS layer with all associated attribute information. Preliminary identification of the collected samples, besides field relations of observed structures and features, was carried out in each station. The samples have been the subject matter of detailed petrographic investigation using the polarizing microscope in order to determine their essential mineral constituents, textural relations, and consequently the exact lithologic nomenclatures.
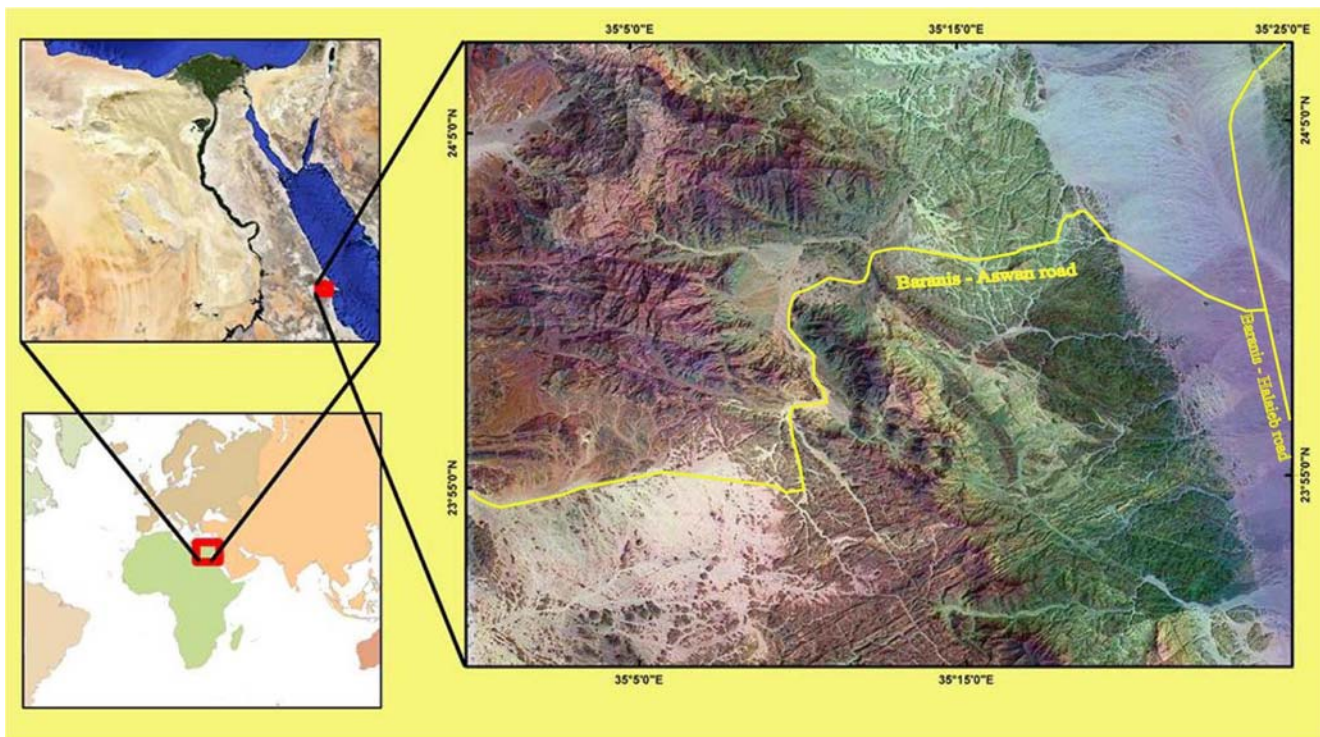
Fig. 1 Location map of the area of West Baranis, Southeastern Desert, Egypt

Workflow of the study

The present study utilized the ASTER data for lithologic discrimination of the exposed lithologies in the study area, with emphasis on the application of band combination, band ratio, and decorrelation stretch. ASTER band combination and band ratios used in previous works and calibrate results with the previous mapping works and field work for purpose drawing a new digital geological map in detail with more discriminate and definite the boundary between various rock units of the study area (Fig. 4).

ASTER image processing

Pre-processing

The crosstalk correction was applied to the SWIR bands of each ASTER image using software supplied by the ASTER GDS (ASTER Science Project Website 2007). The VNIR and SWIR bands were "stacked" into a single file at 30-m resolution. This stacked file was then atmospherically corrected using the FLAASH module in for ENVI. A subset containing only VNIR bands at 15 m was created and also atmospherically corrected using FLAASH.

Processing

False-color-composite images

The false-color-composite technique is extensively used for combining multispectral images through color coding. In fact, it is possible to create a vast number of false-color composites from the ASTER bands. The current study used the validated ASTER band combination (7, 3, 1) in RGB. The latter is equivalent to the Landsat Thematic Mapper (TM) band combination (7, 4, 2) in RGB (Abdeen et al. 2001), which was selected for the global Landsat mosaic created from NASA (Horning 2010). It is useful for outlining lithological units, as well as structural and morphological features (Abdeen et al. 2001), and provides striking imagery for desert regions. The present study depends mainly on this band combination for drawing the base map.

Band-ratio composite image

The band ratio is one of the earliest techniques used in remote sensing images. The band-ratio technique was used to enhance the spectral differences between bands and to decrease the effects of topography. The study used a band-ratio composite image carried out in previous works for areas that resemble the study area lithologically and have the same climate circumstances. These ratios
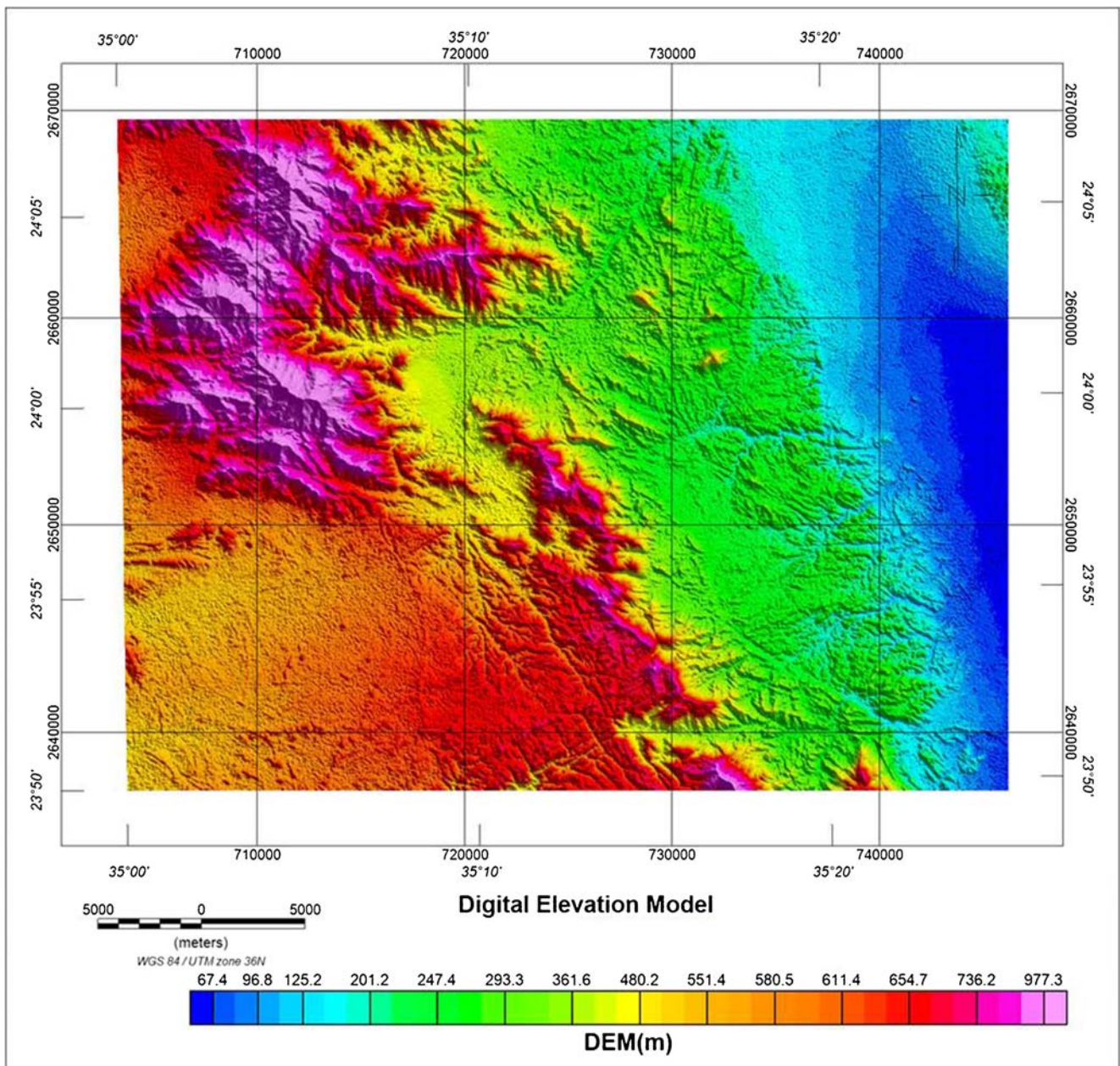
Fig. 2 ASTER GDEM showing the topography of the study area

compared with each other's and at the same time calibrated with data obtained from field investigations, in addition to the previously published geologic maps including the study area. The best band ratios that gave more discrimination to the different rock units in the area were selected.

ASTER-TIR lithologic indices

Based on analysis of TIR spectral properties of typical rocks on the earth, Ninomiya et al. (2005) and Rockwell and Hofstra (2008) proposed several mineralogic indices including quartz index (QI) and mafic index (MI) for de-

Table 1 The ASTER scene characteristics of the study area

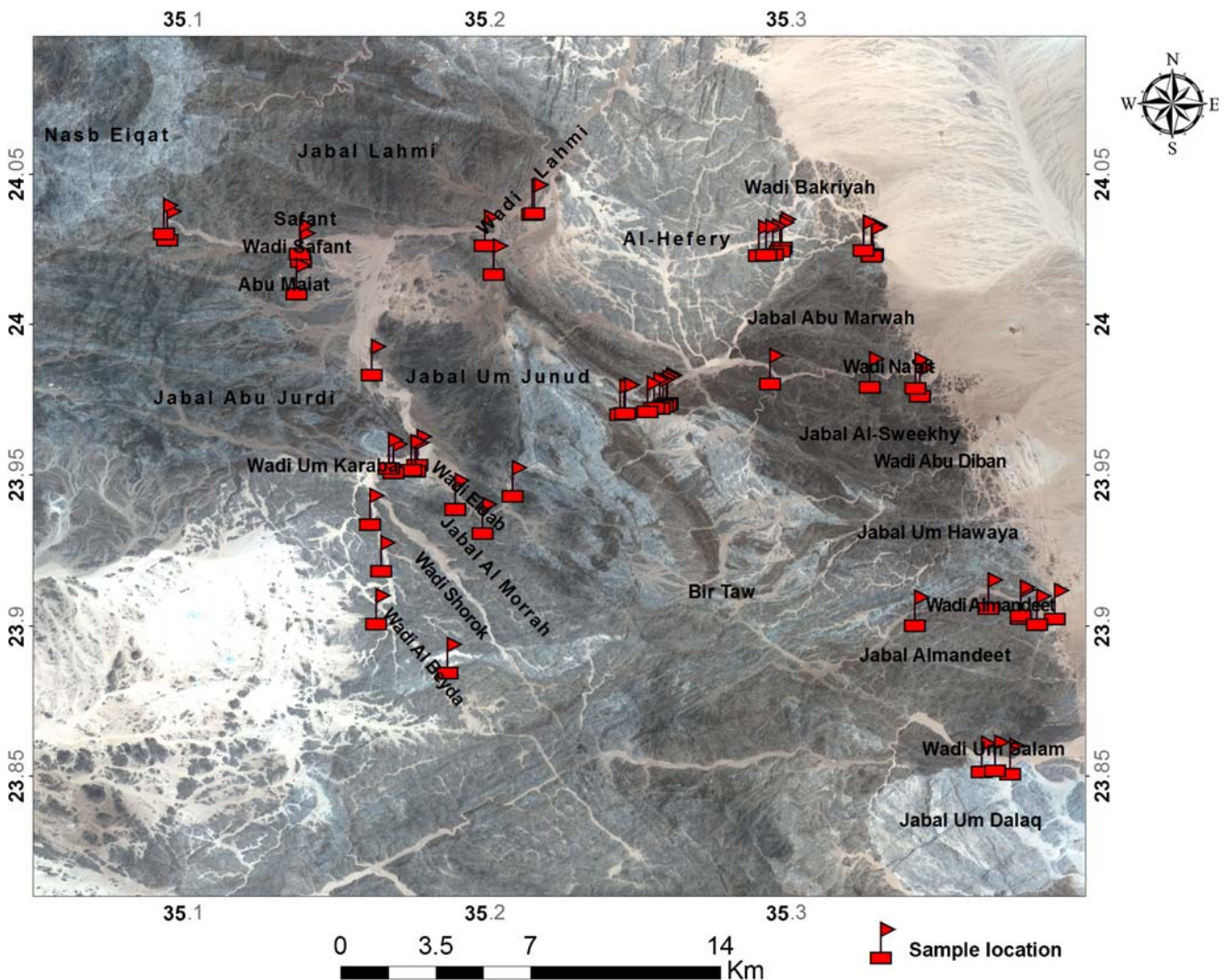| Level	Scene no.	Date of acquisition	Time	Cloud cover
ASTL1B	0105170834061407010020	17 May 2001	08:34:06 a.m.	0%

Fig. 3 Map showing the sample locations

tecting the mineralogic or chemical composition of quartoze, and silicate rocks with ASTER-TIR level 1B (radiance at the sensor) data. These mineralogic indices provide one unified approach for lithologic mapping in arid and semi-arid terranes of the earth. The quartz index (Rockwell and Hofstra,2008) and mafic index (Ninomiya et al.,2005) were applied in the present study area.

Rockwell and Hofstra (2008) introduced the quartz index based on bands 10–13 to enhance the spectral emissivity pattern of quartz, where the quartz index (QI) = (b11/(b10 + b12))*(b13/b12). This ratio is equivalent to a mixture of QI and silicon index (SI) (Gupta 2018). According to Ninomiya et al. (2005), the mafic index, where MI = (band 12 × band 14^3/ band 13^2), is expected to be high for ultramafic rocks and systematically lower as the rock type changes to felsic and finally quartzose rock. The present study relies on the QI and MI for preliminary identification of rock verities in the base map.

Decorrelation stretch

Decorrelation stretch is a way to enhance and reduce redundancy in the images; in other words, it is a process that is used to enhance (stretch) the color differences found in a color image. This process is based upon the removal of inter-channel correlation with each pixel (Alley 1999). It is especially useful when viewing multi-spectral datasets that are highly correlated (e.g., a combination of the SWIR or TIR bands). Applying decorrelation stretch essentially stretched each band such that the minimum correlation between bands is shown and therefore the decorrelation, i.e., areas of the spectrum where bands are not correlated, are highlighted (Kalinowski and Oliver 2004). In the present study area, decorrelation stretching of TIR band combination 14, 12, 10 in RGB was used.
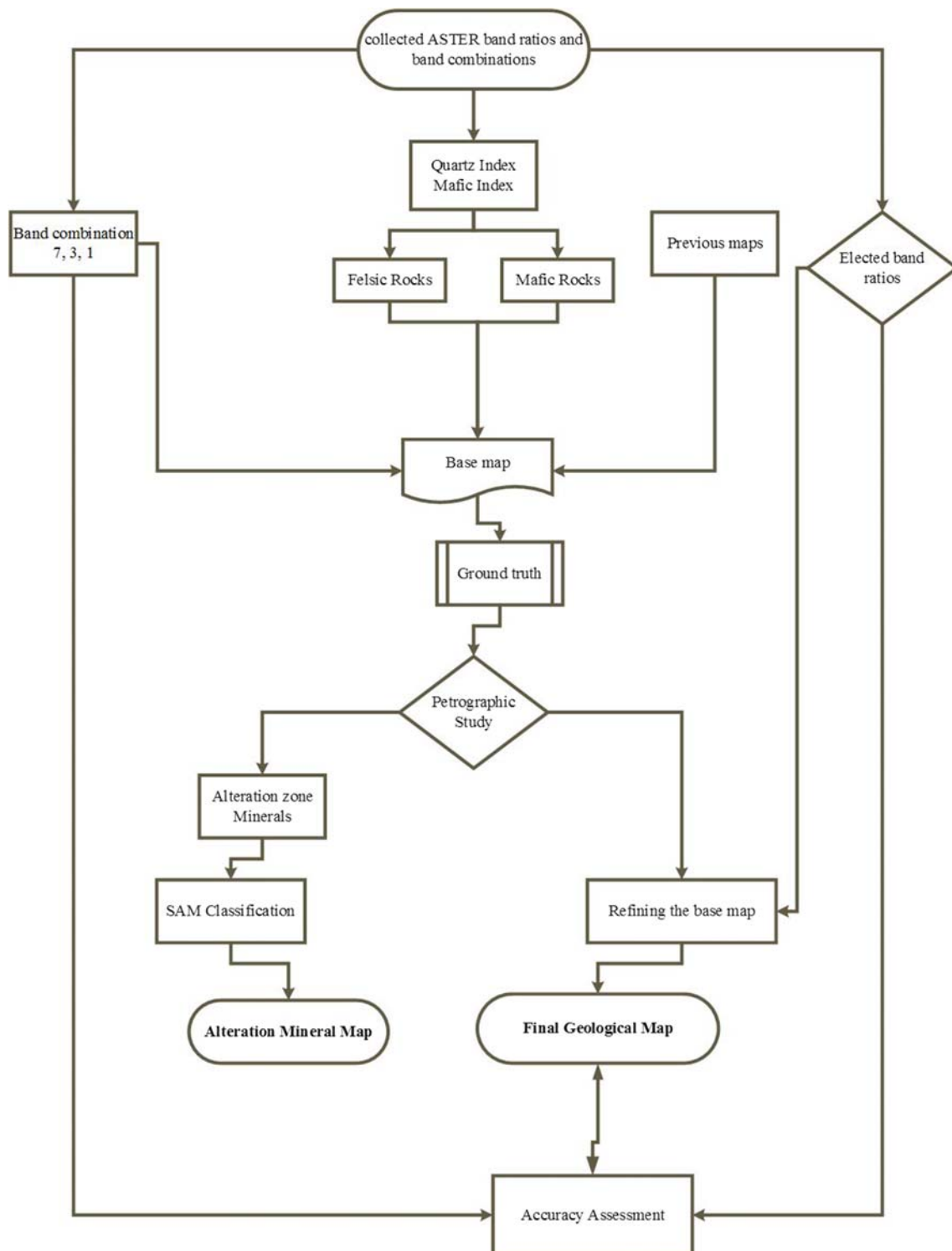
Fig. 4 Flow chart of the methodology used for the present study

Spectral angle mapper

The spectral angle mapping (SAM) technique proposed by Kruse et al. (1993) is a supervised classification that depends on the angles between image pixel spectra and training data (ROIs) or library spectra of selected end members. The

algorithm determines the similarity between two spectra by calculating the spectral angle between them. The SAM output is a classified image whose pixel values represent the alpha (α) angle in radians, which is measured from the reference spectrum for each class. Spectral angle mapping was applied on the normalized spectral data of the selected hydrothermal

alteration minerals (kaolinite, chlorite, and epidote) from the United States Geological Survey (USGS) spectral library, then resampled to ASTER spectral resolution.

Results and discussion

Lithologic mapping using remote sensing data

The present study depends mainly on the ASTER band combination 7, 3, 1 in RGB for drawing the base map. It was useful in discriminating Neoproterozoic lithologic units outcropping in the West Berenice area, particularly NE-oriented dike swarms, as well as biotite granite (Fig. 5).

The color-ratio composite images of 4/8, 4/2, 8/9 in RGB; 4/7, 4/1, 2/3*4/3 in RGB; 7/6, 6/5, 6/4 in RGB; (2 + 4)/3, (5 + 7)/6, (7 + 9)/8 in RGB, and (1 + 3)/2, (3 + 5)/4, (5 + 7)/6 in RGB were used as an aid for compiling the geologic map (Fig. 6a–e). These ratio images were used to enhance the spectral differences between bands and also to reduce the shadow effects caused by topography. The more efficient color-ratio composite images in the study area were 4/1, 3/1, 12/14 in RGB and 4/7, 4/6, 4/10 in RGB (Figs. 7 and 8). The

ASTER color-ratio composite image 4/1, 3/1, 12/14 in RGB is introduced by Abdeen et al. (2001) to map exposed rocks in arid regions (Fig. 8). Kalinowski and Oliver (2004) used this ratio for mapping in the "ASTER Mineral Index Processing Manual." The authors recommended it because of a high optimum index factor (OIF) and the presence of diagnostic spectral features in these bands. The composite image of color ratio 4/1, 3/1, 12/14 in RGB incorporates bands from the VNIR, SWIR, and TIR regions of the electromagnetic spectrum (Abdeen et al. 2001). This ratio was useful in mapping the shared granite as a yellow to a greenish yellow color (Fig. 7). The ASTER color-ratio composite images 4/7, 4/6, 4/10 in RGB proposed by Gad and Kusky (2007) were applied in this study for lithological mapping. This ratio was used to map the area between Wadi Abu Dibban and Jabal Abu Marwah (Fig. 8). It can differentiate between the amphibolite unit and the granodiorite with amphibolite fragments unit, where the amphibolite exhibits a dark pink and dark color, while the granodiorite with the amphibolite fragments unit shows a dark green color (Fig. 8).

The ASTER-TIR indices QI and MI were used for preliminary identification and discrimination of the exposed lithologies. QI and MI were used to differentiate between felsic and
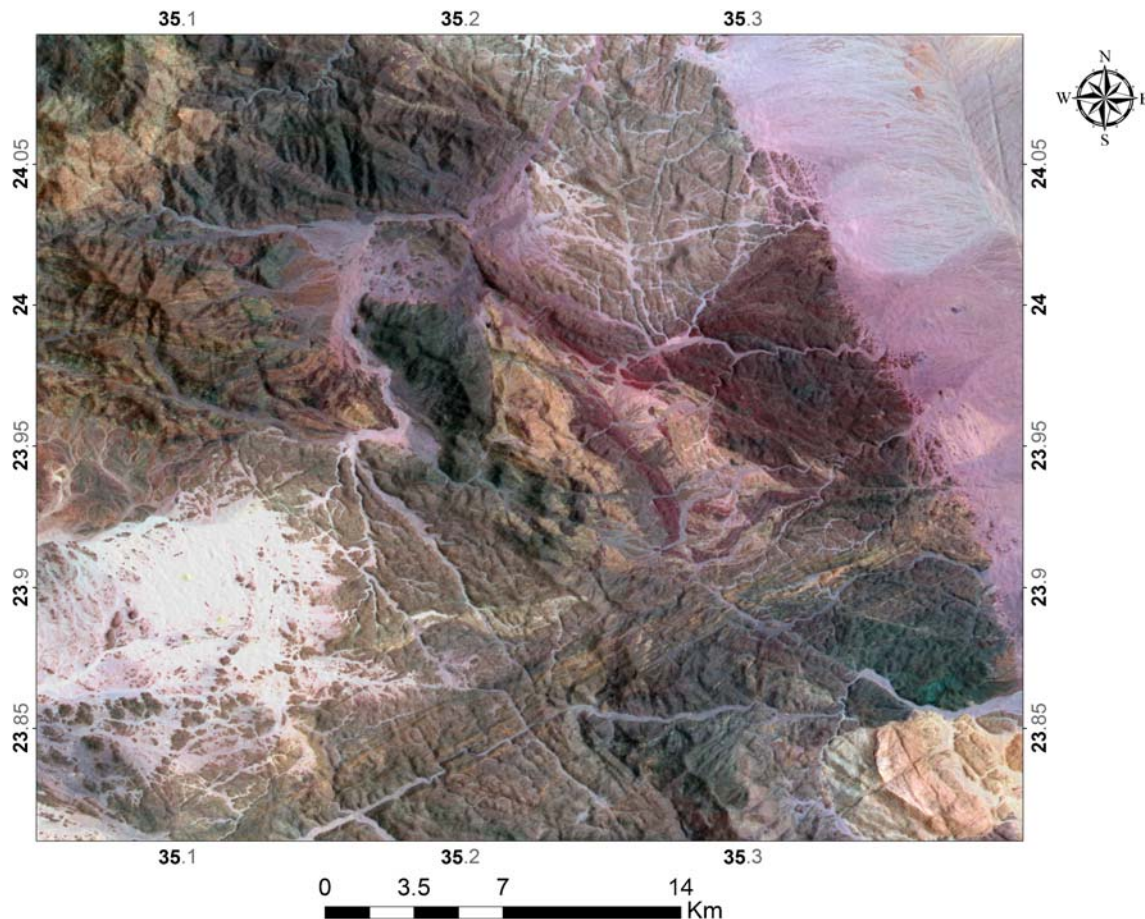

Fig. 5 False-color-composite image of ASTER band combination 7, 3, 1 in RGB
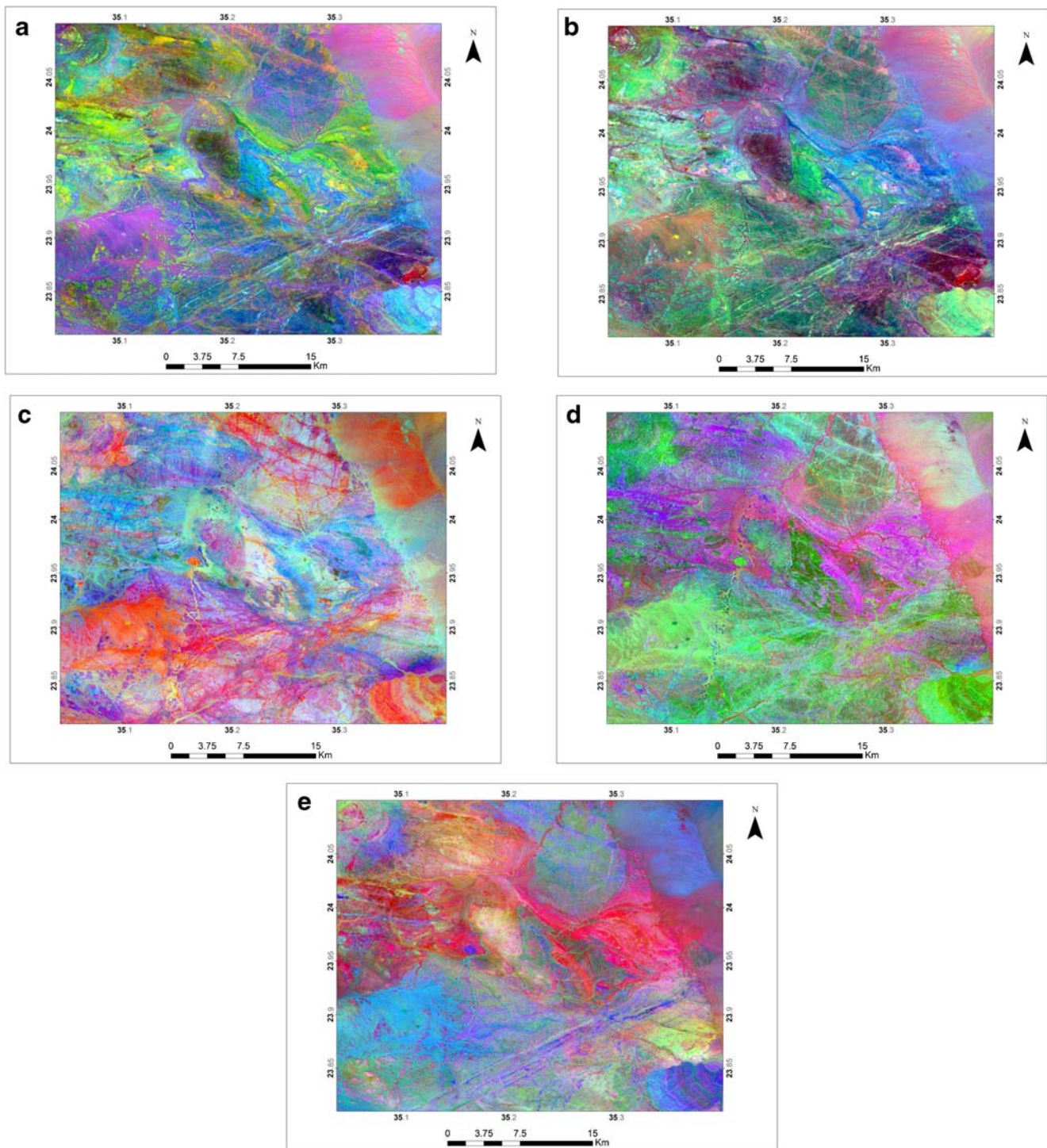
Fig. 6 Color-ratio composite image that was applied on the study area; **a** 4/8, 4/2, 8/9 in RGB; **b** 4/7, 4/1, 2/3*4/3 in RGB; **c** 7/6, 6/5, 6/4 in RGB; **d** (2 + 4)/3, (5 + 7)/6, (7 + 9)/8 in RGB; **e** (1 + 3)/2, (3 + 5)/4, (5 + 7)/6 in RGB

mafic varieties. The study area encompasses wide varieties of rock units such as granite, granodiorite, rhyolite, amphibolite, and metagabro. Rock types such as granite, granodiorite, and rhyolite are felsic, whereas rock types such as amphibolite and metagabro are mafic. The proposed felsic map is created by applying a threshold equal to the mean of the digital number

(DN) of the pixel value on QI (Fig. 9) whereas the mafic map was created by applying a threshold equal to the mean plus the standard deviation of the pixel value on MI (Fig. 9).

Within the West Berenice area, linear enhancement of the 14, 12, 10 in RGB TIR-decorrelation stretch data shows a variety of lithologic compositions ranging from the mostly
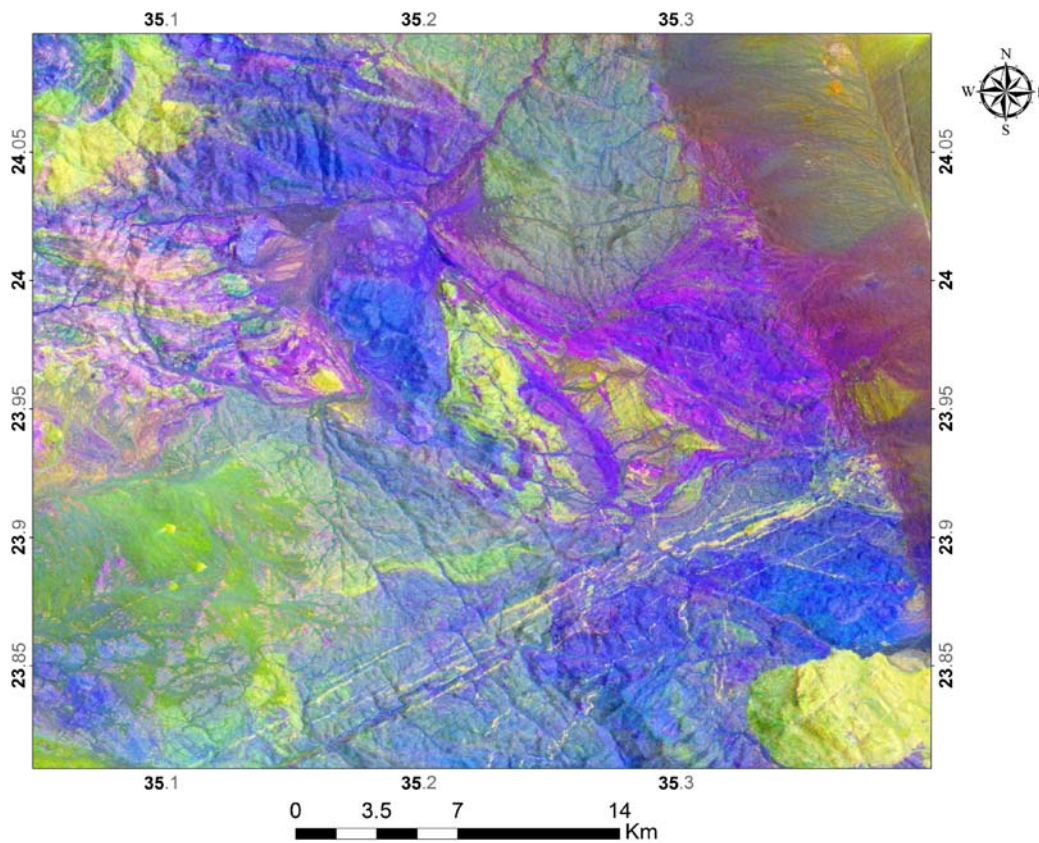
Fig. 7 Color-ratio composite image 4/1, 3/1, 12/14 in RGB

mafic (blue colored), and quartz-rich rocks such as shared granite and gneissose granitoids (umber colored) (Fig. 10).

Field investigation and petrographic studies

The exposed lithologic units in the area are arranged in a chronologic order from oldest to youngest in Table 2. The augen gneisses occur as a relatively small outcrop in the southern continuation of Jabal Abu Jurdi at the linking of Wadi Eidab and Wadi karaba. These gneisses are alternated with "lit-par-lit" amphibolites and sheared granites (Fig. 11a). For the unaided eye, the augen gneisses are fine to medium grained, gray to light pink, with noticeable mica flakes. Under the microscope, they have a granoblastic texture of sutured, mosaicked, and stretched-out granulated quartz masses. They are composed essentially of quartz, plagioclase, biotite, microcline, and hornblende (Fig. 11b).

The amphibolites and hornblende–quartz schist are cropping out at the central eastern and western parts of the study area. In the eastern part, these rocks occupy the flanks of Wadi Abu Diban and extend westwards to Bir Taw, and from Jabal Abu Marwah and Jabal Al-Sweekhy. They extend further northwestwards to cross Wadi Lahami and the entrance of Wadi Safant. In Jabal Abu Jurdi, the amphibolites occur as alternated bands and layers with the sheared granites (Fig. 11c, d). They are gray to dark gray, fine to coarse grained, and in some places, they are remarkably schistose. They are intruded by granite, traversed by mafic dikes and invaded by quartz veins and veinlets that cut across shearing. The amphibolites consist fundamentally of preferably oriented crystals of hornblende, plagioclase, and quartz, together with secondary epidote and calcite, and accessory opaques.

The sheared granites outcrop in several locations in the mapped area, such as in the northwestern part at Jabal Nasb Eiqat. In the central part, they occupy the eastern side of Jabal Um Junud and extend further north from Wadi Abu Diban to reach the western side of Wadi Na'ait. In the southeastern sector of the concerned area, they are encountered at Jabal Um Dalaq. In Jabal Abu Jurdi, the shared granites are alternated with the amphibolites (Fig. 11d, e). For the unaided eye, these rocks are pale brown in color, fine to medium grained, and showing a preferred orientation of quartz and feldspar minerals. Microscopically, they consist of quartz, K-feldspars (microcline and orthoclase), plagioclase, hornblende, and muscovite. Epidote and chlorite of penninite variety are secondary minerals. These constituents are occasionally mylonitized and quartz crystals are frequently highly strained showing strong undulatory extinction. Bending, kinking, and crumpling of plagioclase along with the breaking of K-feldspars are rather evidence supporting a cataclastic effect (Fig. 11f).
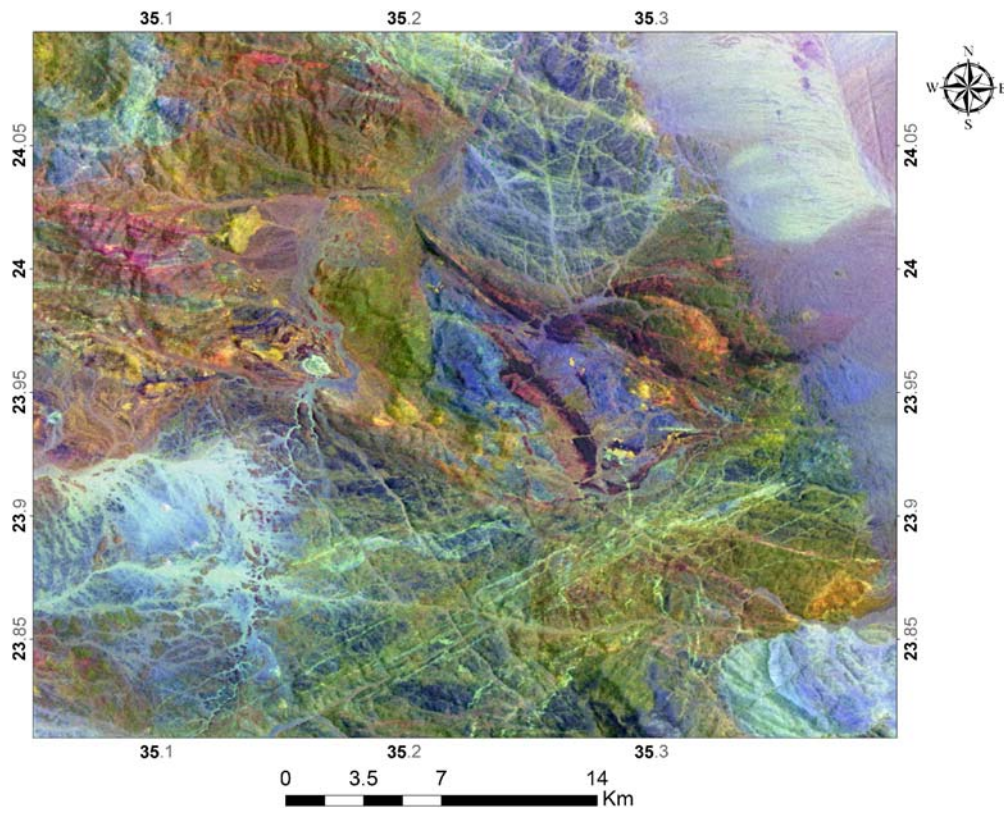
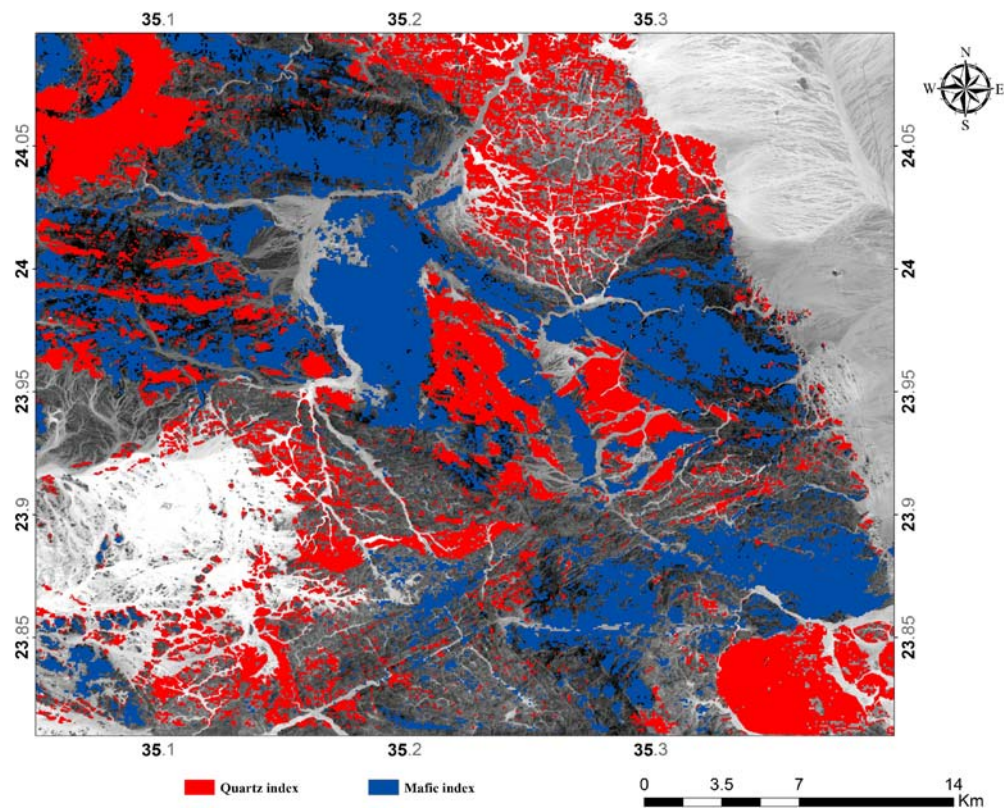Fig. 8   Color-ratio composite image 4/7, 4/6, 4/10 in RGB

Fig. 9   Quartz and mafic indices map using threshold value show the felsic rocks in the study area
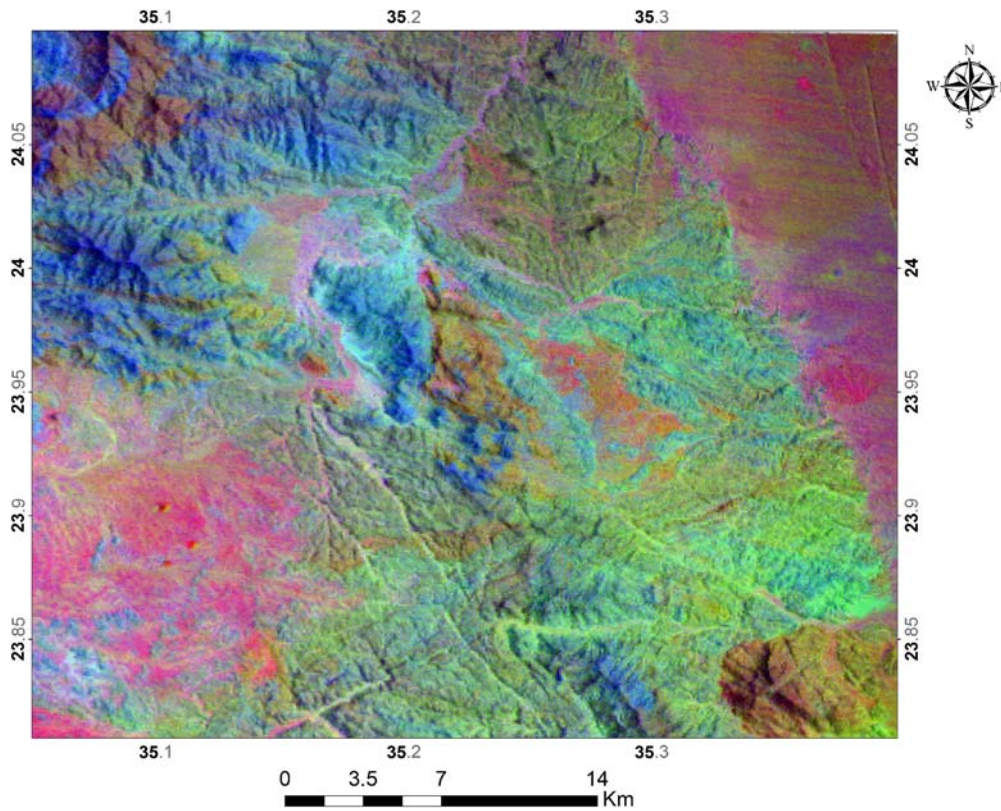
Fig. 10 Decorrelation stretching of TIR band combination 14, 12, 10 in RGB

The metagabbro–diorite complex outcrops at Jabal Almandeet and Jabal Um Hawaya in the southeastern part of the study area, and also at Jabal Lahami in the northern area, in addition to the western side of Jabal Um Junood. These rocks are dark gray in color and medium to coarse grained. They have a massive form and a distinguished spheroid weathering (Fig. 11g). In Jabal Almandeet, they are intruded by rhyolite, and in Jabal Lahami, they are traversed by mafic dikes, and in places, they are injected by quartz veins (Fig. 12a). Microscopically, they consist mainly of plagioclase, actinolitic green hornblende, olivine, and biotite. Epidote (pistachite) and chlorite are secondary minerals. Opaques are accessories (Fig. 12b).

The gneissose granitoids are encountered in the northeastern part of the study area forming Jabal Al-Hefery. These rocks have an oval outcrop and locally form a low to relatively moderate relief country. They are gray in color and medium to coarse grained (Fig. 12c). They are jointed and dissected by basic dikes which mainly trend in the N–S to NNE–SSW directions. They are exfoliated and include xenolithic

Table 2 The exposed rock units in the study area arranged from the youngest to the oldest based on inferred field relations

• Rhyolite (locally microgranite; shear zone related) • Dykes • Perthitic leucogranite • Biotite granite • Tonalite • Granodiorite with amphibolite Fragments • Gneissose granitoids • Metagabbro-Diorite Complex (locally deformed and metamorphosed) • Sheared granites • Amphibolites & Hornblende Quartz Schist • Augen Gneisses	Youngest ↓ Oldest

Fig. 11 **a** Panoramic view showing the augen gneiss outcrop (AG) alternated with amphibolite and shared granite (A/SG). Jabal Abu Jurdi, looking NW. **b** Microphotograph showing the main fabric in the augen gneiss. C.N, X2. **c** Field photograph of an outcrop of amphibolite in Wadi Na'aite. Looking SW. **d** Alternated bands of amphibolite (Am) and shared granite (SG) in Jabal Abu Jurdi. Looking ENE. **e** Shared granite in Jabal Um Junud. Looking E. **f** Microphotograph showing strong mylonitization and cataclasis in sheared granite. C.N, X5. **g** Massive metagabbro with spheroid weathering in Jabal Um Hawaya. Looking N. **h** General view showing mafic dikes traversing the metagabbro (MG) of Jabal Lahmi. Looking NW. **i** Microphotograph showing well-developed olivine (Ol) in metagabbro. The rock is remarkably deformed. C.N, X2

enclaves, which are foreign bodies captured from the surrounding country rocks by the gneissose granitoids body. The xenolith composition is identical to the compositions of surrounding rocks (Fig. 12d). The contacts between the gneissose granitoids and surrounding lithologies are intensively sheared and have semi-vertical foliations. Microscopically,

the gneissose granitoids consist of quartz, plagioclase, hornblende, and biotite. Secondary minerals are epidote and chlorite. Opaques are accessories (Fig. 12e).

The granodiorite with amphibolite fragments is encountered in Jabal Al-Sweekhy and Jabal Abu Marwah. The amphibolite fragments often show a sigmoidal pattern, and their

Fig. 12 **a** General view showing mafic dikes traversing the metagabbro (MG) of Jabal Lahmi. Looking NW. **b** Microphotograph showing well-developed olivine (Ol) in metagabbro. The rock is remarkably deformed. C.N, X2. **c** Gneissose granitoids, Wadi Lahmi. Looking ESE. **d** Top view showing xenolithic fragment of amphibolite (Xn) within the gneissose granitoids (Gn) in Jabal Al-Hefery. **e** Microphotograph showing well-developed gneissosity in the gneissose granodiorite. C.N, X2. **f** Granodiorite (Gd) with amphibolite fragments (AF) dissected by a basic dike, Wadi Na'ait. Looking S

arrangement reflects shearing in the NW direction. They are jointed and intruded by mafic dikes dipping eastward (Fig. 12f).

The tonalite is exposed in the southern continuation of Wadi Albeday and Wadi Shorok (Fig. 13a). Under the microscope, it consists of quartz, microcline, plagioclase, and biotite. Chlorite and epidote are secondary minerals.

The biotite granite occupies a vast domain in the southern part of the mapped area, where it extends in the Jebal Almorrah, Wadi Albeday, and Wadi Shorok areas. The rock is medium to coarse grained, gray in color, massive, and exhibiting exfoliations (Fig. 13b). Microscopically, it consists of plagioclase, microcline, quartz, biotite, and hornblende. Kaolinite and epidote are secondary minerals (Fig. 13c).
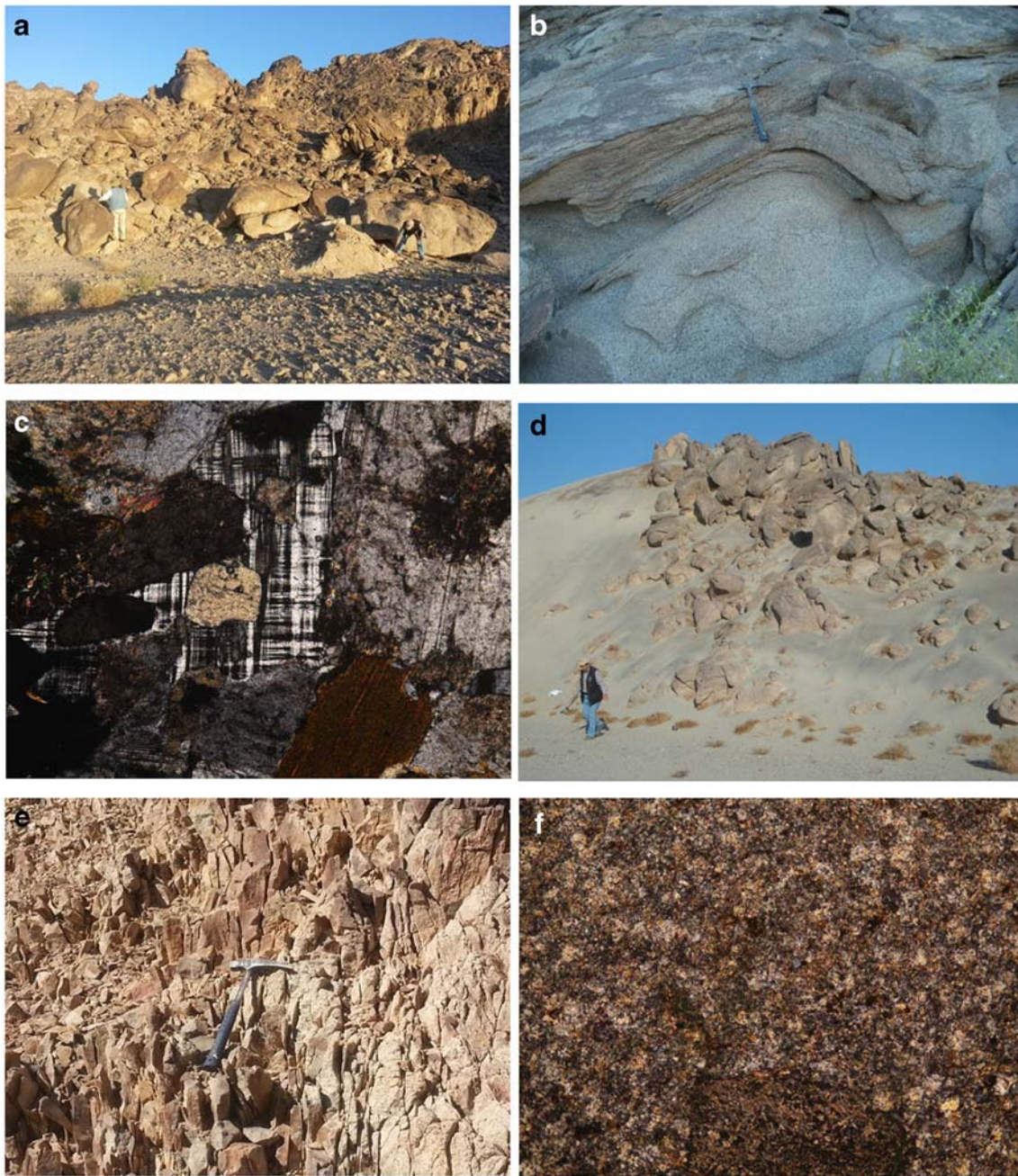
Fig. 13 **a** An outcrop of tonalite cropping out along the flanks of Wadi Albeday. Looking S. **b** Exfoliated biotite granite. Wadi Albeday. Looking NE. **c** Microphotograph showing microcline with cross-hatching twinning poikilitically encloses plagioclase and quartz crystals in biotite granite. C.N, X5. **d** An outcrop of perthitic leucogranite along the flanks of Wadi Almandeet. Looking NW. **e** Highly sheared microgranite. Wadi Almandeet. Looking NW. **f** Microphotograph showing spherulitic texture in rhyolite. C.N, X5

The perthitic leucogranite is encountered as unmappable masses at Jabal Almandeet (Fig. 13d). This rock is medium to coarse grained, pink in color, and massive. Microscopically, it is composed of K-feldspar, plagioclase, quartz, biotite, and hornblende, together with kaolinite. Opaques are accessory minerals.

The rhyolite and microgranite are cropping out in the southeastern part of the mapped area in the form of dike swarms. These dike swarms are shear zone related and are oriented in the ENE–WSW. They extend to a few kilometers and vary in width from few centimeters to more than 40 m. They are pink to red in color, occasionally sheared and trending in the NE direction with nearly vertical dipping. They are highly resistant to weathering compared to the country rocks. The microgranite is fine grained, pink in color, and highly sheared (Fig. 13e). Microscopically, quartz, orthoclase, and plagioclase are the main components. The rock shows a well-developed spherulitic texture (Fig. 13f).
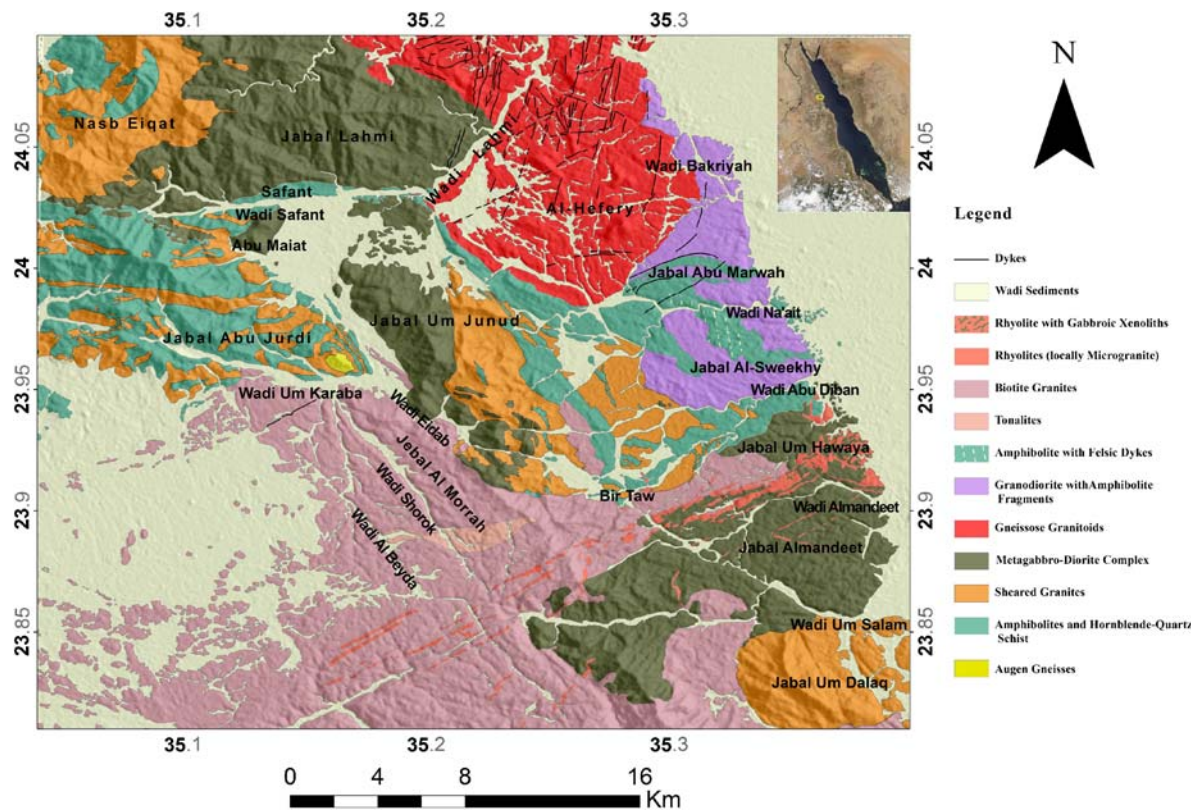
Fig. 14 The final lithologic map of West Berenice was created after integrating the results of false-color-composite images, color-ratio composite images, quartz and mafic index image of ASTER data, and fieldwork
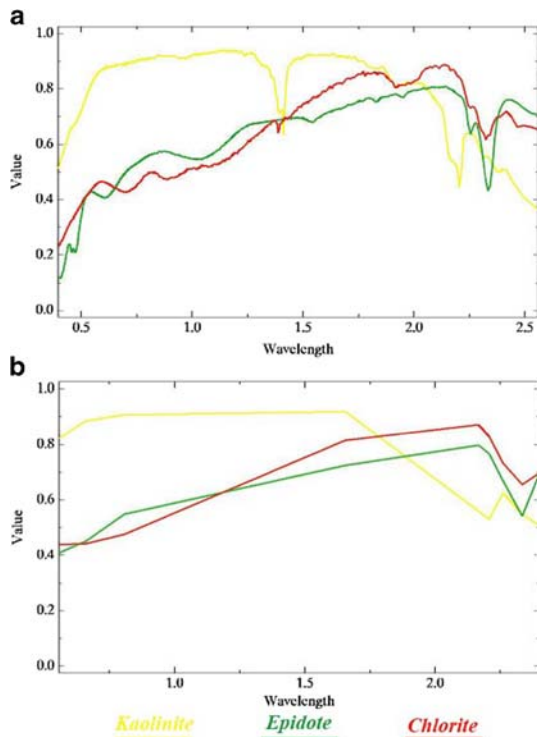

Fig. 15 **a** Spectral data of the selected hydrothermal alteration minerals (kaolinite, chlorite, and epidote) from the United States Geological Survey (USGS) spectral library. **b** End members' spectra resampled to ASTER resolution, used in SAM classification using USGS spectral library for VNIR-SWIR spectral region

The area under investigation was traversed by numerous basic dikes. The most prominent dikes are in the northeast of the study area, where dike swarms extend to few kilometers. Dikes have different colors ranging from black to gray with thickness ranges from some centimeters to a few meters, and the dip of dikes varies from vertical to horizontal. They are trending in various directions but commonly orientated in two major directions, NNE–SSW and ENE–WSW. In many cases, the dikes are fractured, with remarkable epidotization along the dike surface. Some dikes are more resistant to weathering compared to the country rocks, forming well-developed ridges that stand out in relief (Fig. 13a, f).

A geologic map was constructed for the Berenice area with more details and accuracy (Fig. 14). The eleven rock units observed in the geological map have the same nomenclatures with high definition of boundaries. The newly constructed map shows six lithologic units, not recorded in the previously published map by the Egyptian Mineral Resources Authority. These units are augen gneisses, sheared granites, granodiorite with amphibolite fragments, perthitic leucogranite, rhyolite, and microgranite.

Alteration mapping

Microscopic examination of the thin sections revealed that the alteration minerals in the study area include essentially

Table 3 Matching maximum angles (radians) used in SAM classification for ASTER VNIR-SWIR

End member	Maximum angle (rad)
Chlorite	0.13
Kaolinite	0.30
Epidote	0.105

kaolinite, chlorite, and epidote. Spectral angle mapping was applied on the normalized spectral data of the selected hydrothermal alteration minerals (kaolinite, chlorite, and epidote) from the United States Geological Survey (USGS) spectral library (Fig. 15a), then resampled to ASTER spectral resolution (Fig. 15b). Kaolinite and chlorite minerals have a similar absorption feature near 1.4 μm and 2.2 μm (Fig. 15a). This is probably due to the fundamental stretching mode of Al-OH (Hunt 1977). ASTER band 6 (2.185–2.225 μm) covers the wavelength of 2.2 μm whereas the wavelength 1.4 μm is not covered by ASTER bands (Fig. 15b). Epidote has an intensive absorption feature at 2.2 μm and is also covered by ASTER band 6 (Fig. 15a, b). The applied maximum angles for ASTER VNIR-SWIR are listed in Table 3. They were selected according to field determinations and used as the threshold spectral

angle of each end-member mineral, as lower spectral angles represent better matches to the end-member spectra.

The SAM classification by using USGS reference successfully identified kaolinite (yellow color), chlorite (red color), and epidote (green color) (Fig. 16). The kaolinite occurs in the metagabbro and diorite complex southeast of the study area and at the transitional area between granitoid gneiss and metagabbro and around mafic dikes. Chlorite and epidote mostly associated together in the amphibolite and amphibolite schist unit and the granitoid with amphibolite fragments unit in the central area (Fig. 16).

Accuracy assessment

The accuracy assessment was carried out to evaluate the band combination and band ratio classification used in lithologic mapping in this study. To know the accuracy, we classified the band ratio and band combination images by the supervised maximum likelihood classification method. The purpose of classification is to produce thematic maps where each pixel in the image is assigned based on spectral response to a
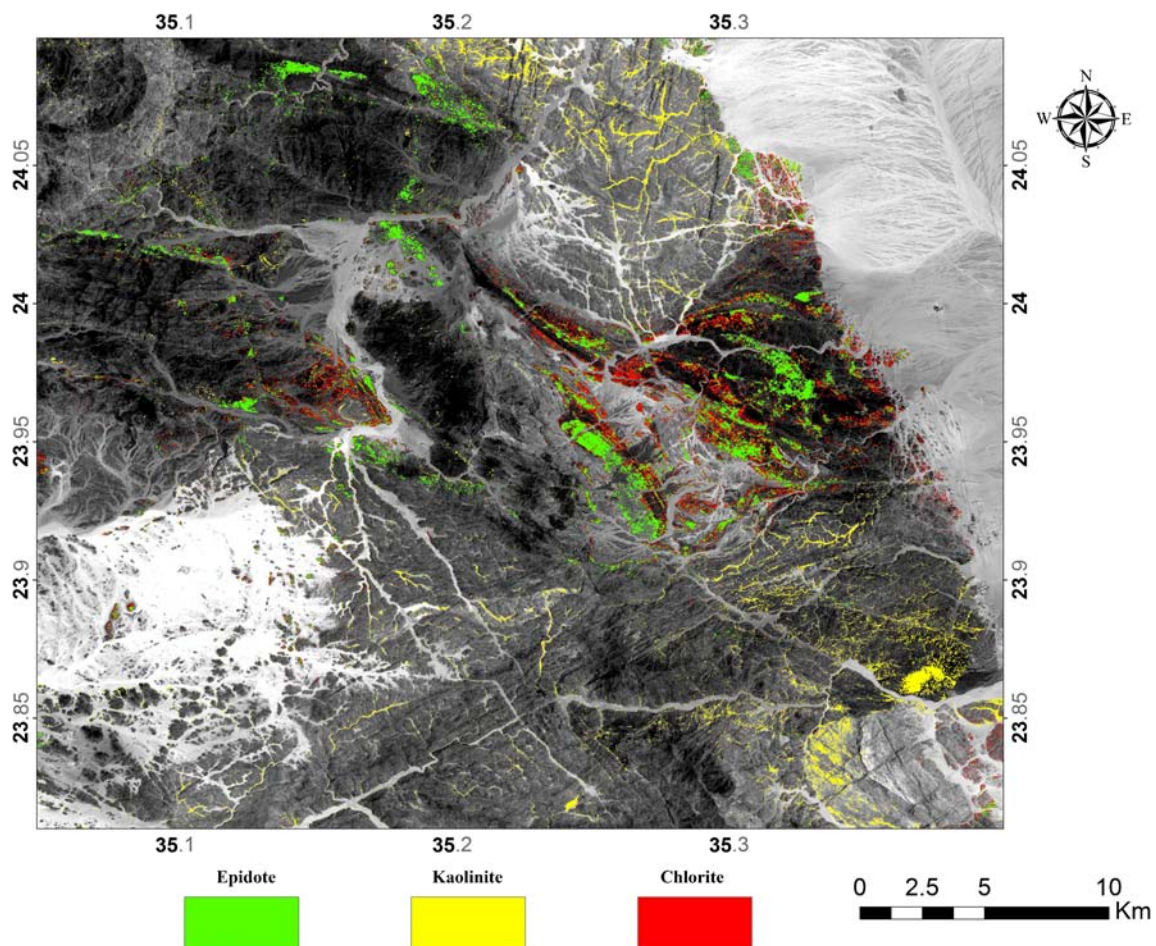

Fig. 16 ASTER band 1 image with mapped alteration zones manifesting as red for chlorite, yellow for kaolinite, and green for epidote
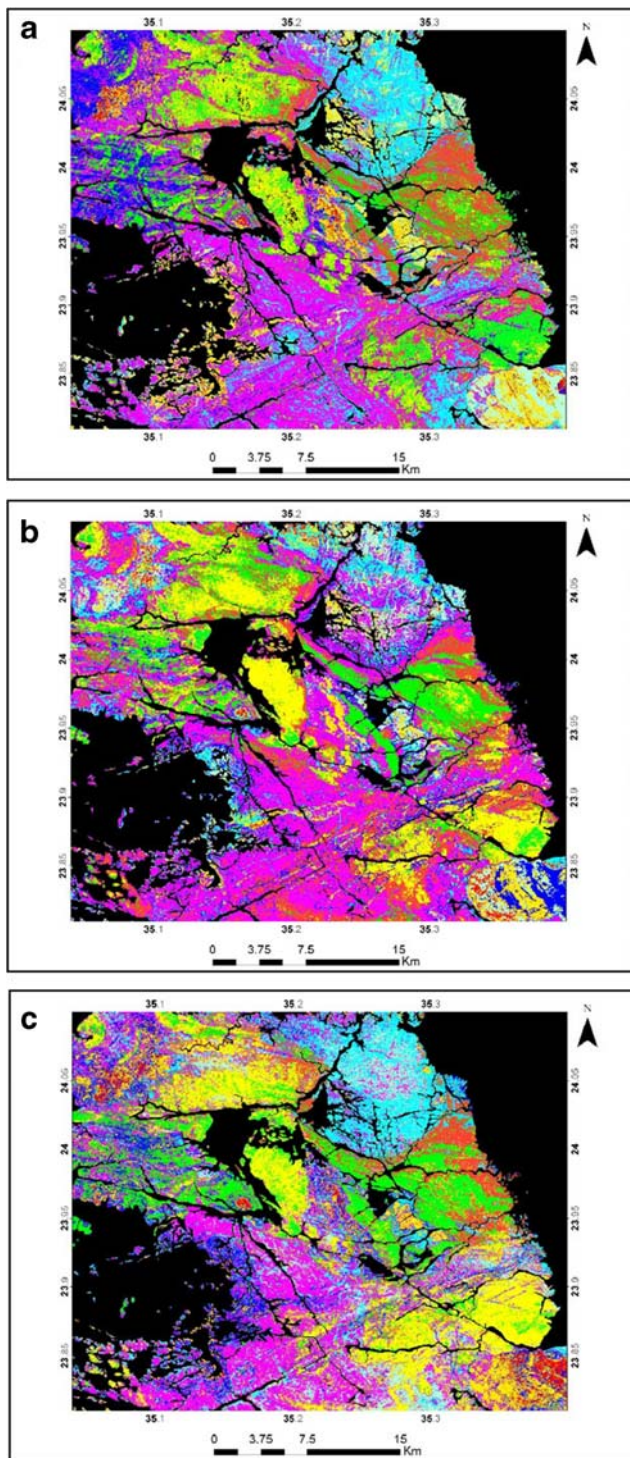
Fig. 17 **a** Supervised classification for band combination 7, 3, 1 in RGB. **b** Supervised classification for band ratio combination 4/7, 4/6, 4/10 in RGB. **c** Supervised classification for band ratio combination 4/1, 3/1, 12/14 in RGB

particular theme (Gupta 2018). Additionally, the overall accuracy of resulting classified images was assessed based on the true dataset using a confusion matrix (Sun et al. 2019). However, wadi sediments are masked to be the classification

exclusively in the basement outcrops. Supervised classification is based on detection algorithms using pixels from known position samples located within a scene as a basis for comparison to other pixels from objects in the same scene. Each pixel is assigned to the class that has the highest probability. When the highest probability is smaller than a specified threshold, the pixel stays unclassified. There were about one hundred GPS points, which were mainly used with some random point and used to evaluate the classification processes.

We use Confusion Matrix in ENVI software to find out the total accuracy and kappa (K) statistics of thematic maps that result from supervised classifications of the band combination and band ratios that were used in mapping by comparing each classification result with ground truth information that reached to more than one hundred GPS points.

Consequently, the total accuracy average in the band combination 7, 3, 1 in RGB (Fig. 17a and Table 4) was 63.5%, while the accuracy average in-band ratio 4/7, 4/6, 4/10 in RGB (Gad and Kusky 2007) was 78.6% (Fig. 17b and Table 5). The total accuracy of band ratio 4/1, 3/1, 12/14 in RGB (Abdeen et al. 2001) was 85.01% (Fig. 17c and Table 6).

Summary and conclusions

Regular field geological mapping provides excellent fact information and actuality data; however, it is expensive, time consuming, and ineffective for lithologic mapping. This paper focuses on integrated remote sensing data, geological field investigation, and petrographic studies to provide reasonable high-resolution lithological discrimination of the Neoproterozoic lithologic units outcropping in the West Berenice area, situated in the Southeastern Desert of Egypt. The applied remote sensing techniques embrace false-color-composite images, color-ratio composite image, ASTER-TIR lithologic indices, decorrelation stretch, and spectral angle mapper (SAM).

The processed ASTER image 7, 3, 1 in RGB was used for preliminary discrimination of geological units and trace contacts. The lithological units of the study area were verified in the field and mapped in detail in the digital map. The area forms a mosaic from basement rocks (augen gneisses, amphibolites, and hornblende–quartz schist, sheared granites, metagabbro–diorite complex, gneissose granitoids, granodiorite with amphibolite fragments, tonalite, biotite granite, perthitic leucogranite, rhyolite, and microgranite, and dikes) (Table 4).

The integration between the band combination technique and the previous geological mapping allows discriminating between different lithologies. Some authors applied several ratio images to map the basement rocks in areas that have climate circumstances resembling those of the study area. Herein, we use the same techniques, i.e., rationing, with the ground truth data to refine the base map and to construct an accurate and

Table 4 Confusion matrix of user's and producer's accuracies and kappa coefficient of the supervised classification image of the band combination 7, 3, 1

	S. granite	Meta gabbro	Gneiss	B. granite	Tonalite	Masked	Amphib.	A gneiss	Granodiorite	Am-felsic	Rhyolite	Sediments	Total
S. granite	0	21	0	2	0	0	0	3	0	0	14	0	40
Metagabbro	0	87	0	0	0	0	0	0	0	0	0	0	87
Gneiss	0	0	99	0	0	0	0	0	0	0	0	0	99
B. granite	0	2	1	11	0	0	0	0	0	1	0	0	15
Tonalite	0	0	1	39	0	0	0	1	0	0	7	0	48
Masked	0	0	0	0	0	422	0	0	0	0	0	0	422
Amphibolite	0	1	0	0	0	0	111	00	3	0	0	0	115
A gneiss	0	0	0	0	0	0	0	55	0	0	0	0	55
Granodiorite	0	0	0	0	0	0	1	0	22	32	0	0	55
Am-felsic	0	244	0	0	0	0	0	0	1	7	0	0	252
Rhyolite	30	0	3	15	18	0	0	5	0	0	0	0	71
Sediments	45	0	0	0	16	0	0	0	0	0	0	68	129
Total	75	355	104	67	34	422	112	64	26	40	21	68	1388

Overall accuracy = (882/1388) 63.5447%, kappa coefficient = 0.5778

more reliable geological map. Discrepancies among ratio images may help in recognizing the strength/weakness of using a certain ratio for a certain mapping assignment. The band ratio 4/1, 3/1, 12/14 in RGB is the best compared to other used band ratios, where the accuracy reaches (85.01%.). It is recommended to integrate several differentiated band ratio images for a successful detailed geological mapping.

Samples collected from different lithologies outcropping in the concerned area were petrographically investigated. Kaolinite, chlorite, and epidote are the most dominant alteration minerals. Using reference spectra of the USGS spectral library, the spectral angle mapper (SAM) as a supervised classification method was applied for mapping alteration zones in the study area. The kaolinite occurs in the metagabbro and diorite complex unit at the southeastern part of the study area and the transitional area between granitoid gneiss and metagabbro and around mafic dikes. Chlorite and epidote mostly associated together in the amphibolite and amphibolite schist unit and the granitoid with the amphibolite fragments unit.

Table 5 Confusion matrix of user's and producer's accuracies and kappa coefficient of the supervised classification image of the band ratio 4/7, 4/6, 4/10

	S. granite	Meta gabbro	Gneiss	B. granite	Tonalite	Masked	Amphib.	A gneiss	Granodiorite	Am-felsic	Rhyolite	Sediments	Total
S. granite	2	0	2	34	0	0	17	0	0	0	0	0	55
Metagabbro	0	340	0	0	0	0	0	0	4	21	0	0	365
Gneiss	1	0	70	15	0	0	0	2	0	0	4	0	92
B. granite	0	0	0	18	0	0	0	0	0	1	0	0	19
Tonalite	0	0	26	0	0	0	0	0	0	0	0	0	26
Masked	0	0	0	0	0	422	0	0	0	0	0	0	422
Amphibolite	0	0	0	0	0	0	89	0	5	18	0	0	112
A gneiss	12	0	0	0	13	0	0	55	0	0	0	0	80
Granodiorite	0	3	0	0	0	0	0	0	17	0	0	0	20
Am-felsic	0	12	0	0	0	0	0	0	0	0	0	0	12
Rhyolite	4	0	6	0	9	0	0	7	0	0	17	7	50
Sediments	56	0	0	0	12	0	6	0	0	0	0	61	135
Total	75	355	104	67	34	422	112	64	26	40	21	68	1388

Overall accuracy = (1091/1388) 78.6023%, kappa coefficient = 0.7381

Table 6 Confusion matrix of user's and producer's accuracies and kappa coefficient of the supervised classification image of the band ratio 4/1, 3/1, 12/14

	S. granite	Meta gabbro	Gneiss	B. granite	Tonalite	Masked	Amphib.	A gneiss	Granodiorite	Am-felsic	Rhyolite	Sediments	Total
S. granite	38	0	0	0	5	0	0	1	0	0	11	0	55
Metagabbro	0	328	0	0	0	0	0	0	0	6	0	0	334
Gneiss	0	0	100	13	0	0	0	0	0	0	0	5	118
B. granite	0	25	0	4	0	0	0	0	0	0	1	0	30
Tonalite	8	0	0	4	10	0	0	0	0	0	4	0	26
Masked	0	0	0	0	0	422	0	0	0	0	0	0	422
Amphibolite	0	1	0	0	0	0	89	0	0	1	0	0	91
A gneiss	4	0	0	0	0	0	0	63	0	0	0	0	67
Granodiorite	0	0	0	0	0	0	0	0	26	1	0	0	27
Am-felsic	0	1	0	0	0	0	23	0	0	32	0	0	56
Rhyolite	25	0	0	46	19	0	0	0	0	0	5	0	95
Sediments	0	0	4	0	0	0	0	0	0	0	0	63	67
Total	75	355	104	67	34	422	112	64	26	40	21	68	1388

Overall accuracy = (1180/1388) 85.0144%, kappa coefficient = 0.8180

In the new given geologic map, additional lithologic units are observed including augen gneisses, sheared granites, granodiorite with amphibolite fragments, perthitic leucogranite, rhyolite, and microgranite. These units do not exist in the previously published map of the area by the Egyptian Mineral Resources Authority.

References

Abdeen MM, Thurmond AK, Abdelsalam MG, and Stern RJ (2001) Application of ASTER band-ratio images for geological mapping in arid regions: the Neoproterozoic Allaqi Suture, Egypt. In *Proceedings of GSA 2001* Annual Meeting. Boston

Abdel-Khalek, M. L., Takla, M. A., Sehim, A., Hamimi, Z., and El Manawi, A. W., 1992. Geology and tectonic evolution of Wadi Beitan area, southeastern Desert, Egypt. *Geology of the Arab World*. Cairo University, 369–394

Aboelkhair H, Ninomiya Y, Watanabe Y, Sato I (2010) Processing and interpretation of ASTER TIR data for mapping of rare-metal-enriched albite granitoids in the Central Eastern Desert of Egypt. J Afr Earth Sci 58(1):141–151

Abrams M, Hook S, Ramachandran B (2002) ASTER user handbook, version 2. Jet propulsion laboratory 4800:135

Akaad , M. K., and El-Ramly , M. F., 1960. Geological history and classification of the basement rocks of the central Eastern Desert of Annals of the Geological Survey of Egypt, Paper. 9, 24pp

Akaad MK, Noweir AM (1969) Lithostratigraphy of the Hammamat umm Seleimat district, Eastern Desert, Egypt. Nature 223:284

Akaad MK, Noweir AM (1980) Geology and lithostratigraphy of the Arabian desert orogenic belt of Egypt between latitudes 25° 35′ and 26° 30′ N. Precambrian Res 6:A6

Alley, R. (1999). Algorithm theoretical basis document for: decorrelation stretch

Amer R, Kusky T, El Mezayen A (2012) Remote sensing detection of gold related alteration zones in Um Rus area, Central Eastern Desert of Egypt. Adv Space Res 49(1):121–134

Amer R, Kusky T, Ghulam A (2010) Lithological mapping in the Central Eastern Desert of Egypt using ASTER data. J Afr Earth Sci 56(2–3):75–82

Askari G, Pour A, Pradhan B, Sarfi M, Nazemnejad F (2018) Band ratios matrix transformation (BRMT): a sedimentary lithology mapping approach using ASTER satellite sensor. Sensors 18(10):3213

Asran AM, Emam A, El-Fakharani A (2017) Geology, structure, geochemistry and ASTER-based mapping of Neoproterozoic Gebel El-Delihimmi granites, Central Eastern Desert of Egypt. Lithofacies 282:358–372

ASTER Science Project Website, 2007. http://www.gds.aster.ersdac.or.jp/

Bedini E (2019) Application of WorldView-3 imagery and ASTER TIR data to map alteration minerals associated with the Rodalquilar gold deposits, southeast Spain. Adv Space Res 63(10):3346–3357

Conoco, C., 1987. Geological map of Egypt, scale 1: 500,000-NF 36 NE-Bernice, Egypt. The Egyptian General Petroleum Corporation, Cairo.

Di Tommaso I, Rubinstein N (2007) Hydrothermal alteration mapping using ASTER data in the Infiernillo porphyry deposit, Argentina. Ore Geol Rev 32(1–2):275–290

El Ramly MF (1972) A new geological map for the basement rocks in the eastern and southwestern desert of Egypt: scale 1: 1,000,000. *Annals of the Geological Survey of Egypt*

El Gaby S (1988) Geology, evolution and metallogenesis of the Pan-African belt in Egypt. The Pan-African belt of the northeast Africa and adjacent areas, 17–68

El Gaby S, List FK, and Tehrani R (1990) The basement complex of the Eastern Desert and Sinai. S. Rushdi (Ed.) The geology of Egypt, Balkema, Rotterdam, pp. 175–184

Elsaid M, Aboelkhair H, Dardier A, Hermas E, Minoru U (2014) Processing of multispectral ASTER data for mapping alteration minerals zones: as an aid for uranium exploration in Elmissikat-Eleridiya granites, Central Eastern Desert, Egypt. The Open Geology Journal 8(1)

Gabr SS, Hassan SM, Sadek MF (2015) Prospecting for new gold-bearing alteration zones at El-Hoteib area, South Eastern Desert, Egypt, using remote sensing data analysis. Ore Geol Rev 71:1–13

Gabr S, Ghulam A, Kusky T (2010) Detecting areas of high-potential gold mineralization using ASTER data. Ore Geol Rev 38(1–2):59–69

Gad S, Kusky T (2007) ASTER spectral ratioing for lithological mapping in the Arabian–Nubian shield, the Neoproterozoic Wadi Kid area, Sinai, Egypt. Gondwana Res 11(3):326–335

Gupta RP (2018) Remote sensing geology. 3rd Edition, Springer-Verlag GmbH Germany, 428

Hassan SM, Taha MM, Mohammad AT (2017) Late Neoproterozoic basement rocks of Meatiq area, Central Eastern Desert, Egypt: petrography and remote sensing characterizations. J Afr Earth Sci 131:14–31

Horning N (2010) Remote sensing for ecology and conservation: a handbook of techniques. Oxford University Press

Hume WF (1934) Geology of Egypt, Vol. 2, part I. The metamorphic rocks. Geol. Surv. Egypt, Cairo

Hunt GR (1977) Spectral signatures of particulate minerals in the visible and near infrared. Geophysics 42(3):501–513

Ibrahim WS, Watanabe K, Yonezu K (2016) Structural and litho-tectonic controls on Neoproterozoic base metal sulfide and gold mineralization in North Hamisana shear zone, South Eastern Desert, Egypt: the integrated field, structural, Landsat 7 ETM+ and ASTER data approach. Ore Geol Rev 79:62–77

Jakob S, Bühler B, Gloaguen R, Breitkreuz C, Eliwa HA, El Gameel K (2015) Remote sensing based improvement of the geological map of the Neoproterozoic Ras Gharib segment in the Eastern Desert (NE–Egypt) using texture features. J Afr Earth Sci 111:138–147

Johnson PR, Andresen A, Collins AS, Fowler AR, Fritz H, Ghebreab W, Stern RJ (2011) Late Cryogenian–Ediacaran history of the Arabian–Nubian shield: a review of depositional, plutonic, structural, and tectonic events in the closing stages of the northern East African Orogen. J Afr Earth Sci 61(3):167–232

Kalinowski A, Oliver S (2004) ASTER mineral index processing manual. Remote Sensing Applications, Geoscience Australia 37:36

Kruse FA, Lefkoff AB, Boardman JW, Heidebrecht KB, Shapiro AT, Barloon PJ, Goetz AFH (1993) The spectral image processing system (SIPS)—interactive visualization and analysis of imaging spectrometer data. Remote Sens Environ 44(2–3):145–163

Ninomiya Y, Fu B, Cudahy TJ (2005) Detecting lithology with advanced spaceborne thermal emission and reflection radiometer (ASTER) multispectral thermal infrared "radiance-at-sensor" data. Remote Sens Environ 99(1–2):127–139

Ninomiya Y, Fu B (2018) Thermal infrared multispectral remote sensing of lithology and mineralogy based on spectral properties of materials. Ore Geol Rev

Noori L, Pour AB, Askari G, Taghipour N, Pradhan B, Lee CW, Honarmand M (2019) Comparison of different algorithms to map hydrothermal alteration zones using ASTER remote sensing data for Polymetallic vein-type ore exploration: Toroud–Chahshirin Magmatic Belt (TCMB), North Iran. Remote Sensing 11(5):495

Pour AB, Hashim M, Hong JK, Park Y (2019a) Lithological and alteration mineral mapping in poorly exposed lithologies using Landsat-8 and ASTER satellite data: North-Eastern Graham Land, Antarctic Peninsula. Ore Geol Rev 108:112–133

Pour AB, Park Y, Crispini L, Läufer A, Kuk Hong J, Park TYS, Zoheir B, Pradhan B, Muslim AM, Hossain MS, Rahmani O (2019b) Mapping Listvenite occurrences in the damage zones of northern Victoria land, Antarctica using ASTER satellite remote sensing data. Remote Sensing 11(12):1408

Pour AB, Park Y, Park TYS, Hong JK, Hashim M, Woo J, Ayoobi I (2019c) Evaluation of ICA and CEM algorithms with Landsat-8/ASTER data for geological mapping in inaccessible regions. Geocarto Int 34(7):785–816

Pour AB, Park Y, Park TYS, Hong JK, Hashim M, Woo J, Ayoobi I (2018a) Regional geology mapping using satellite-based remote sensing approach in northern Victoria land, Antarctica. Polar Science 16:23–46

Pour AB, Hashim M, Park Y, Hong JK (2018b) Mapping alteration mineral zones and lithological units in Antarctic regions using spectral bands of ASTER remote sensing data. Geocarto Int 33(12):1281–1306

Rockwell BW, Hofstra AH (2008) Identification of quartz and carbonate minerals across northern Nevada using ASTER thermal infrared emissivity data—implications for geologic mapping and mineral resource investigations in well-studied and frontier areas. Geosphere 4(1):218–246

Salem SM, El Sharkawi M, El-Alfy Z, Soliman NM, Ahmed SE (2016) Exploration of gold occurrences in alteration zones at Dungash district, Southeastern Desert of Egypt using ASTER data and geochemical analyses. J Afr Earth Sci 117:389–400

Schurmann HME (1957) The Precambrian of Egypt east of the River Nile. Geol and Minjbeuw, 19th year, No. 5, 165–171

Sheikhrahimi A, Pour AB, Pradhan B, Zoheir B (2019) Mapping hydrothermal alteration zones and lineaments associated with orogenic gold mineralization using ASTER data: a case study from the Sanandaj-Sirjan zone, Iran. Adv Space Res 63(10):3315–3332

Stern RJ (1994) Arc assembly and continental collision in the Neoproterozoic East African Orogen: implications for the consolidation of Gondwanaland. Annu Rev Earth Planet Sci 22(1):319–351

Stern RJ (2002) Subduction zones. Rev Geophys 40(4):3–1

Sun T, Chen F, Zhong L, Liu W, Wang Y (2019) GIS-based mineral prospectivity mapping using machine learning methods: a case study from Tongling ore district, eastern China. Ore Geol Rev 109:26–49

Zoheir B, Emam A (2012) Integrating geologic and satellite imagery data for high-resolution mapping and gold exploration targets in the south Eastern Desert, Egypt. J Afr Earth Sci 66:22–34

Zoheir B, El-Wahed MA, Pour AB, Abdelnasser A (2019) Orogenic gold in transpression and transtension zones: field and remote sensing studies of the Barramiya–Mueilha sector. Egypt Remote Sens 11:2122